Journal of Turbulence
Vol. 00, No. 00, 2011, 1–14

RESEARCH ARTICLE

Estimation and prediction of the roughness function on realistic surfaces

J. Yuan* and U. Piomelli

Queen's University, Kingston, Ontario K7L 3N6, Canada

(*Received 00 Month 200x; final version received 00 Month 200x*)

Large-eddy simulations are carried out in turbulent open-channel flows to determine the roughness function and the equivalent sand-grain roughness height, k_s, over sand-grain roughness and different types of realistic roughness replicated from hydraulic turbine blades. A range of Reynolds numbers and mean roughness heights is chosen, leading to both transitionally and fully rough regimes. The start of the fully rough regime is shown to depend on the roughness type, and k_s depends strongly on the surface topography. We then examine several existing correlations that predict k_s based on the information of the surface geometry. In the cases where the surface slope is an important parameter, the moments of surface height statistics do not predict the roughness function, while the existing forms of slope-based correlations perform well. The range of applicability of various correlations is shown to vary with the roughness topography, as the critical value of the effective slope, separating the waviness and roughness regimes, is shown to be higher for a realistic surface, compared to the value for the more regular types of roughness that were previously studied.

Keywords: turbulent flows, boundary layers, large-eddy simulations, roughness

1. Introduction

1.1. *Roughness effects*

Roughness occurs everywhere, from buildings and canopies, to engineering surfaces with erosion, deposits, and spallations [1]. Rough-wall effects on the flow are summarized by Raupach *et al.* [2] and Jimenez [3]. They include an offset of the mean-velocity profile, quantified by the roughness function, ΔU^+, the intensification of Reynolds stresses, more isotropic distribution of turbulent kinetic energy (TKE) into its three components, and the alteration of the near-wall turbulent structures. In the case of high Reynolds number and small roughness length scale (compared to the boundary layer thickness), the roughness effects on the turbulence are limited to a near-wall layer called the "roughness sublayer" [3]. The outer-layer turbulent statistics remain unchanged when normalized using the friction velocity u_τ; this is called "outer-layer similarity".

Experimental and numerical studies are usually carried out on surfaces with uniform distributions of elements of standard shapes, such as spheres, bars, cylinders and so on, although more realistic surfaces have been considered recently [4–6]. Realistic roughness differs from regular (or "modelled") roughness: it is characterized by a wider spectrum of wavelengths and random distribution of structures of each scale. Wu and Christensen [5] compared different patches of turbine-blade roughness and observed significant dependence of the most intense ejection and

---

*Corresponding author. Email: junlin.yuan@queensu.ca

ISSN: 1468-5248 (online only)

DOI: 10.1080/14685248.YYYYxxxxxx
http://www.tandfonline.com

sweep events on the surface topography. In later investigations [7, 8], they showed that outer-layer similarity also applies to realistic roughness; specifically, to the mean velocity, Reynolds normal and shear stresses, and the overall spatial structure of the outer-layer turbulence agree with the smooth-wall flow. Christensen and co-workers [9, 10] compared a full surface and its lower-order representation and found that the larger surface scales predominantly determine the roughness effects on the turbulent statistics and the instantaneous turbulent events; however, the lower-order surface does not reproduce well the most intense ejection and sweep events in the roughness sublayer. Licari and Christensen [11] conducted experiments to study turbine roughness reconstructed from a subset of the surfaces scales, and found that both the small and large scales contribute to the enhancement of turbulence. Anderson and Meneveau [12] showed that, as smaller scales of a fractal roughness are progressively included, the friction keeps increasing, indicating a difference in the friction on modelled roughness compared to a realistic one, which includes smaller scales. Recently, transitionally rough flows have been studied by Busse *et al.* [13], who performed direct numerical simulations (DNS) in open-channel flows on several types of realistic surface; they also observed that drag depends on the three-dimensional topography of the surfaces and is not solely determined by the physical roughness height.

1.2. *Equivalent sand-grain height*

These results show that the topographical features of rough surfaces play a role in affecting the strong, energy-producing turbulence events near the wall, and thus affect the drag. Therefore, simulations of rough-wall flows should take into account detailed features of the surface. Common numerical approaches to include roughness effects include: (1) direct or large-eddy simulations (DNS or LES) with a body-fitted mesh or immersed boundary methods (IBM), which resolve the detailed surface but require high computational cost; (2) the discrete-element method (DEM), which does not resolve the surface but involves major modifications of the governing equations, and has been shown to work mainly for small-scale roughness structures and roughness peaks (other than valleys) [14], whereas a realistic roughness is often characterized by multiple scales and coexistence of peaks and valleys; and (3) rough-wall correction to the turbulence models for the Reynolds-Averaged Navier-Stokes (RANS) equations, which models roughness effects without physically resolving the surface or changing the basic equations.

In RANS solvers, the single parameter used to describe the roughness is the equivalent sand-grain height, k_s, which relates the drag of an arbitrary type of roughness to that of the uniform sand-grain roughness studied by Nikuradse [15]. What can be usually measured, however, is the mean height, $\overline{k}$. The drag depends on both $\overline{k}$ and the roughness texture; these two factors combine to determine k_s. For a given surface type, *i.e.*, a set of surfaces with the same texture, k_s depends on $\overline{k}$ alone. To relate $\overline{k}$ of an arbitrary surface to its k_s, one uses the mean velocity profile in the logarithmic region assuming fully rough flows: over the Nikuradse sand grains, the mean velocity is

$$U^+(y^+) = \frac{1}{\kappa}\ln\left(y/k_s\right) + 8.5, \tag{1}$$

while for an arbitrary surface, it is

$$U^+(y^+) = \frac{1}{\kappa}\ln\left(y/\overline{k}\right) + C, \tag{2}$$

where C depends on the surface type. A superscript "+" indicates normalization using u_τ and the viscous length-scale, δ_ν. Equating the right-hand-sides of Equations (1) and (2) gives that $k_s/\overline{k}$ is a constant dependent on the surface texture. Note that this linear relation between k_s and $\overline{k}$ applies to the fully rough regime only.

1.3. *Prediction of equivalent sand-grain height*

Correlations have been proposed to predict the constant $k_s/\overline{k}$ solely based on the geometric characteristics of the surface. Reviews are found in Bons [16] and Flack and Schultz [6]. A set of commonly used correlation is based on the surface slope. For instance, Sigal and Damberg [17] and van Rij *et al.* [18] proposed

$$\ln\left(\frac{k_s}{\overline{k}}\right) = a\ln(\Lambda_s) + b, \tag{3}$$

where

$$\Lambda_s = \left(\frac{S}{S_f}\right)\left(\frac{S_f}{S_s}\right)^{-1.6}, \tag{4}$$

and S, S_f, and S_s are the reference surface area before adding roughness, the total frontal area of the roughness, and the total windward wetted surface, respectively; hence Λ_s contains both slope and shape information for the surface. Reasonable collapse was obtained for gas-turbine roughness using this correlation [4]. Note that other forms of Λ_s have been proposed for regular 2D or 3D roughness [19–21], but the form in Equation (4) is best adapted for realistic surface. The constants a and b are empirical coefficients. Another correlation of this type was proposed by Bons [22]; it is based on the root-mean-square of local surface slope, α_{rms}:

$$\frac{k_s}{\overline{k}} = a\alpha_{\mathrm{rms}}^2 + b\alpha_{\mathrm{rms}}, \tag{5}$$

where α is the local streamwise slope angle, which can be easily obtained from a 1D surface trace.

A second class of correlations is based on the moments of height statistics, including the second (k_{rms}), the third (skewness, s_k), and sometimes higher-order moments (kurtosis, k_u); one of these correlations was proposed by Flack and Schultz [6] and was shown to work well on several types of realistic surfaces (gravel, honed surfaces, *etc.*):

$$\frac{k_s}{\overline{k}} = a\frac{k_{\mathrm{rms}}}{\overline{k}}(1 + s_k)^b. \tag{6}$$

The "effective slope" (ES) of a surface is an additional parameter that can be used to categorize the roughness types with regards to the importance of surface slope. It is defined as

$$ES = \frac{1}{L}\int_L \left|\frac{dk(x)}{dx}\right| dx, \tag{7}$$

where $k(x)$ is the height array (obtained from a 1D trace of the surface), x is the streamwise direction, and L is the surface length in x. For modelled roughness constructed with closely packed pyramids [23] and with random sinusoidal waves [24], it has been shown that the surface slope is an important parameter only when the surface is not sufficiently steep: when $ES < 0.35$ ("waviness regime"), ΔU^+ is sensitive to ES, and does not scale with the roughness height. When $ES \geq 0.35$ ("roughness regime"), on the other hand, the surface slope does not affect the drag, and ΔU^+ can be predicted using Equation (6) [6]. The categorisation using ES is of industrial interests, since ES is easy to obtain, and indicates in which regime the surface falls; then a correlation appropriate for this regime can be chosen to predict k_s. Therefore, a general guideline for choosing the k_s-correlation for an arbitrary roughness is possible, if the critical ES value (separating the waviness and roughness regimes) is known for the given type of roughness.

It is the purpose of this paper to (1) investigate the performance of existing correlations in the waviness regime using large-eddy simulations of fully rough flows, and (2) modify the surfaces artificially to obtain a wide range of ES to study the dependence of the critical ES on surface topography. To this end, we simulate open-channel flows over realistic roughness replicated from hydraulic turbine blades. The problem set-up and numerical techniques are first introduced in Section 2; then the mean flow and turbulent statistics are studied in Section 3.1 to validate the simulations; the estimation method for k_s is discussed in Section 3.2, and the evaluation of the k_s-correlations is carried out in Section 3.3; finally, the critical ES is studied in Section 3.4. Conclusions and recommendations for future work will follow in Section 4.

2. Problem formulation

2.1. *Governing equations and numerical techniques*

The incompressible flow of a Newtonian fluid is governed by the equations of conservation of mass and momentum:

$$\frac{\partial \overline{u}_i}{\partial x_i} = 0, \tag{8}$$

$$\frac{\partial \overline{u}_i}{\partial t} + \frac{\partial \overline{u}_i \overline{u}_j}{\partial x_i} = -\frac{\partial \overline{P}}{\partial x_i} + \nu \nabla^2 \overline{u}_i + \frac{\partial \tau_{ij}}{\partial x_i}. \tag{9}$$

x_1, x_2 and x_3 (or x, y and z) are, respectively, the streamwise, wall-normal and spanwise directions, and $\overline{u}_i$ (or $\overline{u}$, $\overline{v}$ and $\overline{w}$) are the filtered velocity components in those directions; $P = p/\rho$ is the modified pressure, ρ the density and ν the kinematic viscosity. The sub-grid stress $\tau_{ij} = \overline{u_i u_j} - \overline{u}_i \overline{u}_j$ is modeled using the Lagrangian-averaged eddy-viscosity model [25], due to the capability of this model to capture spatial flow-heterogeneity by tracking the fluid particle-paths in time. The overbar denoting the filtering operation is hereafter omitted for simplicity. The simulations are performed using a well-validated code that solves (8) and (9) on a staggered grid using second-order, central differences for all terms, a second-order semi-implicit time advancement, and MPI (Message Passing Interface) parallelization [26].

An open-channel flow is simulated with no-slip and symmetric boundary conditions applied to the bottom wall and to the top boundary, respectively. Periodic conditions are used in both the x- and z-directions. An immersed-boundary method is used to impose no-slip boundary condition on the rough surfaces. It is based on the volume-of-fluid approach [27]: the volume fraction occupied by the fluid, $\phi(x, y, z)$, of each cell is calculated in pre-processing. In the current fractional-

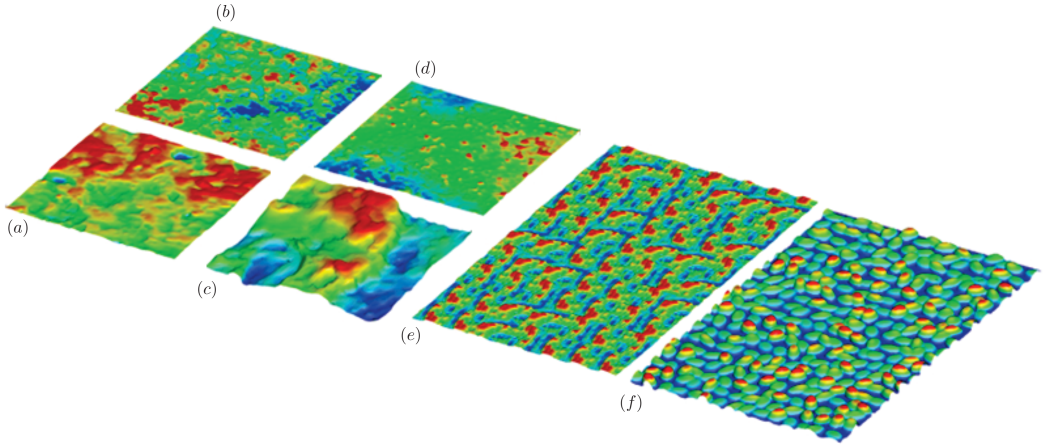

Figure 1. Visualization of (a)–(d) a single tile of four surfaces denoted by S1, S2, S3, S4, (e) a complete surface formed from S3 tiles, and (f) 1/4 of a complete sand-grain (SG) surface. Colouring is based on $y/\overline{k}$.

step framework, a body force, F_i in the x_i direction, is obtained from the velocity predicted without the forcing term, $\widehat{u}_i'$, and the time step, Δt,

$$F_i(x, y, z) = -(1 - \phi(x, y, z))\frac{\widehat{u}_i'(x, y, z)}{\Delta t}. \tag{10}$$

By including F_i into the right hand size of Equation (9) in the actual prediction step, the actual predicted velocity, $\widehat{u}_i(x, y, z)$, at the boundary cell is reduced by $(1 - \phi)$. The eddy viscosity is reduced by $(1 - \phi)$ to account for the decrease of the sub-grid length scale. The forces are distributed in the boundary cells of roughness, and are zero inside the roughness. The force $F_1(x, y, z)$ is integrated throughout the domain to obtain the total drag on a surface, *i.e.*, the sum of both pressure and viscous drag. A detailed description of the numerical method can be found in Yuan and Piomelli [27].

2.2. *Surfaces*

The various surface segments and a complete surface used in the present study are shown in Figure 1(a–e). The iso-surface of $\phi = 0.5$, representative of the solid surface, is coloured by the wall-normal location. Each surface is produced from a rectangular patch of roughness, called a "tile" (Figures 1(a–d)). For the current study of generic realistic roughness, it is assumed that the surface characteristics are homogeneous, *i.e.*, there is no preferential tile direction; this assumption applies to a wide range of surfaces, but, under some circumstances, roughness generated by fluid flow can show preferential direction.

To produce the surface, first, the tile is scaled, preserving all length ratios, to match the target average height $\overline{k}$. Then, it is duplicated in both x and z directions to achieve a horizontal domain of size at least $6h \times 3h$. Random rotation ($\alpha_{\text{rotation}} = N\pi/2$, where $N = 0,\ 1,\ 2,$ or 3) is applied to the tiles during the duplication, to achieve homogeneous surface characteristics. A linear smoothing function is applied to the interface between two patches to ensure a seamless match between tiles, and also surface periodicity in the x- and z-directions. An example of the final surface (from S3 tiles) is shown in Figure 1(e). For the sand-grain (SG) roughness, we use the roughness model proposed by Scotti [28]: the virtual sand-paper is constructed from randomly oriented and distributed ellipsoids of the same shape and size (with the three semi-axes of the ratio 1 : 1.5 : 2); one quarter of a complete SG surface is shown in Figure 1(f).

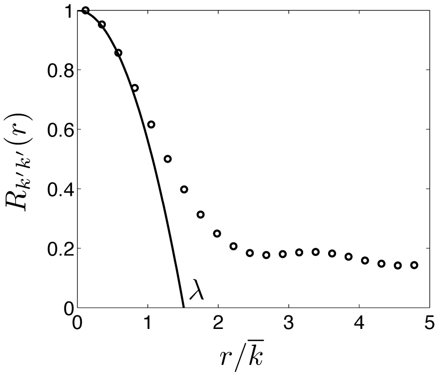

Figure 2. Autocorrelation function $R_{k'k'}$ (○) of surface height fluctuations, as a function of the separation r normalized by mean height, and the parabola $R_{para}(r)$ (——) fitted to determine the Taylor microscale λ of the surface height fluctuations. Case SGk3 is shown.

Table 1. Statistics of rough surfaces.

Surface type	$k_{\mathrm{rms}}/\overline{k}$	s_k	k_u	ES	Λ_s	α_{rms} (in radians)
SG	0.452	0.462	2.867	0.379	39	0.281
S1	0.199	-0.024	3.226	0.104	675	0.109
S2	0.378	0.135	2.561	0.085	1176	0.091
S3	0.419	0.198	2.021	0.164	288	0.147
S4	0.324	0.239	3.413	0.086	1158	0.101

To predict accurately the flow on a surface that represents homogeneous roughness, (1) each tile needs to be well resolved, and (2) the number of tiles should be sufficient to reproduce the random distribution and rotation of surface structures. To ensure that both conditions are met, we choose the cut-off length scale of the surface to be $o(1/10)$ of the Taylor microscale, λ, of the surface height fluctuations, since λ is a good indication of the size of an equivalent "roughness element" in the context of realistic roughness. The calculation of λ is similar to the determination of the Taylor microscale of turbulent fluctuations: first the autocorrelation of the surface height fluctuations, $R_{k'k'}(r)$, is determined as a function of separation, r, in x or z (Figure 2); then a parabola, $R_{para}(r)$, is fitted to the $R_{k'k'}$ profile, *i.e.*,

$$R_{para}(r) = Ar^2 + 1, \tag{11}$$

where the numerical factor A is determined from equaling $(d^2R_{para}/dr^2)|_{r=0}$ to $(d^2R_{k'k'}/dr^2)|_{r=0}$. Once the parabolic profile is known, λ is obtained as the separation at which $R_{para} = 0$.

As will be shown in Table 2, the shape of the characteristic structures of the surface ($\sim o(\lambda)$) is resolved, and our computational power allows each domain to contain around 60^2 samples of structure of the size λ^2—a sufficient sample pool to produce relatively random distribution and rotation of structures of this size.

The characteristic parameters of all surfaces are tabulated in Table 1. SG and S3 have the steepest surface slopes (high values of ES and α_{rms}, and low values of Λ_s). Surfaces SG and S4 give relatively high values of positive s_k, indicating the peaky nature of the surfaces, whereas S1, with negative s_k, is valley-dominated. For all surfaces, the kurtosis is close to 3, indicating that randomness is achieved.

2.3. *Parameters*

The domain size in x and z ranges approximately from $6h \times 3h$ to $12h \times 12h$. This size is sufficient to accommodate the largest turbulent structures on a smooth-wall

Table 2. Spatial resolution in x- and z-directions for all cases.

Surface type	Symbol	grid points per λ	total grid points ($n_i \times n_k$)	Δx^+	Δz^+
Smooth	—	–	$128 \times 128 - 128 \times 192$	$18 - 47$	$9 - 10$
SG	◁	$4 \times 9 - 6 \times 12$	$256 \times 256 - 512 \times 512$	$9 - 15$	$4 - 11$
S1	○	$9 \times 9 - 13 \times 13$	$384 \times 256 - 640 \times 384$	$4 - 17$	$4 - 17$
S2	□	$7 \times 7 - 9 \times 9$	$256 \times 128 - 512 \times 256$	$10 - 42$	$10 - 42$
S3	△	$6 \times 8 - 10 \times 13$	$384 \times 256 - 640 \times 384$	$3 - 21$	$3 - 16$
S4	▷	$8 \times 8 - 11 \times 10$	$256 \times 128 - 384 \times 256$	$7 - 30$	$7 - 30$

channel flow; on 3D regular roughness or realistic gas-turbine surfaces, roughness has been found not to affect the size of large-scale structures in the outer layer [8, 29].

To cover both transitionally rough and fully rough regimes, two Reynolds numbers and three average roughness heights are used: for $Re_\tau = 400$, $\overline{k} = 0.020h$ (k_1), $0.040h$ (k_2), and $0.067h$ (k_3); for $Re_\tau = 1000$, $\overline{k} = 0.040h$ (k_2), and $0.067h$ (k_3). The maximum height ($k_{\max}$, or the peak-to-valley height) varies from $0.03h$ to $0.14h$. $\overline{k}$, normalized by the momentum thickness, ranges between 0.2 and 0.68, slightly lower or similar to values used in other studies on turbine-blade roughness [14, 30]. The spatial resolutions are tabulated in Table 2. Note that the variation of Δx^+ and Δz^+ for each surface is the result of variations of both the Reynolds number and the roughness height. The grid sizes Δx^+ and Δz^+ range between 3 and 40, similar to the values used in previous rough-wall simulations using the same numerical techniques [27]; the resolution in y satisfies $\Delta y^+ < 1$ in the region $y \leq k_{\max}$ and $\Delta y^+ < 25$ at the top boundary; the friction coefficient $C_f = 2(Re_\tau/Re_b)^2$ (where Re_b is the Reynolds number based on the mean bulk velocity) in the smooth cases is within 0.2% of Dean's correlation [31]. The total number of grid points ranges from 128×128 to 640×512 in x and z, and from 82 to 300 in y.

The equations are integrated in time for approximately $100h/u_\tau$ after a steady state is achieved. In the following, the angle brackets $\langle\cdot\rangle$ denote quantities that are averaged in time and over the homogeneous directions, x and z. $U_i(y)$ is the time- and space-averaged velocity

$$U_i(y) = \langle u_i(x, y, z, t)\rangle. \tag{12}$$

The turbulent fluctuation u_i' are calculated by subtracting the time-averaged velocity from the total one:

$$u_i'(x, y, z, t) = u_i(x, y, z, t) - \langle u_i(x, y, z, t)\rangle_t, \tag{13}$$

where $\langle\cdot\rangle_t$ denote only averaging over time. Statistical convergence within 1% is achieved for the mean velocity and second moments statistics.

3. Results

In this section, the cases with k_2 and $Re_\tau = 1000$ are first used to investigate the effects of roughness geometry on the mean flow and the turbulent stresses (Section 3.1); then, the start of the fully rough regime is identified for each of the present surfaces, and $k_s/\overline{k}$ is determined (Section 3.2); k_s is then used to evaluate existing k_s-correlations (Section 3.3), and the critical ES is studied in Section 3.4.

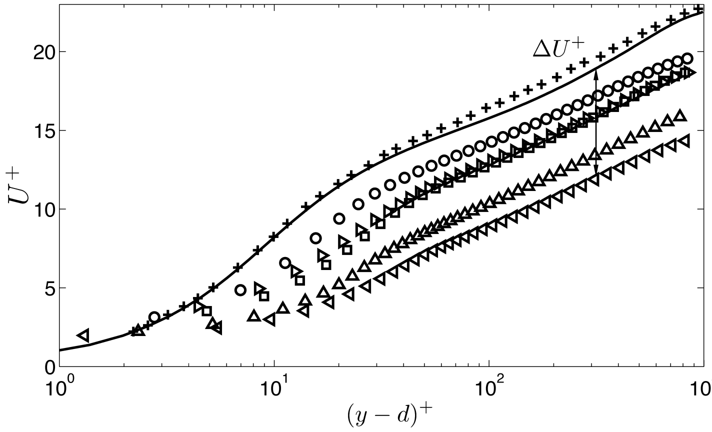

Figure 3. Profiles of streamwise mean velocity in cases with $\overline{k} = k_2$ and $Re_\tau = 1000$. + Smooth-wall experiment [32], ——— smooth, ◁ SG, ○ S1, □ S2, △ S3, ▷ S4.

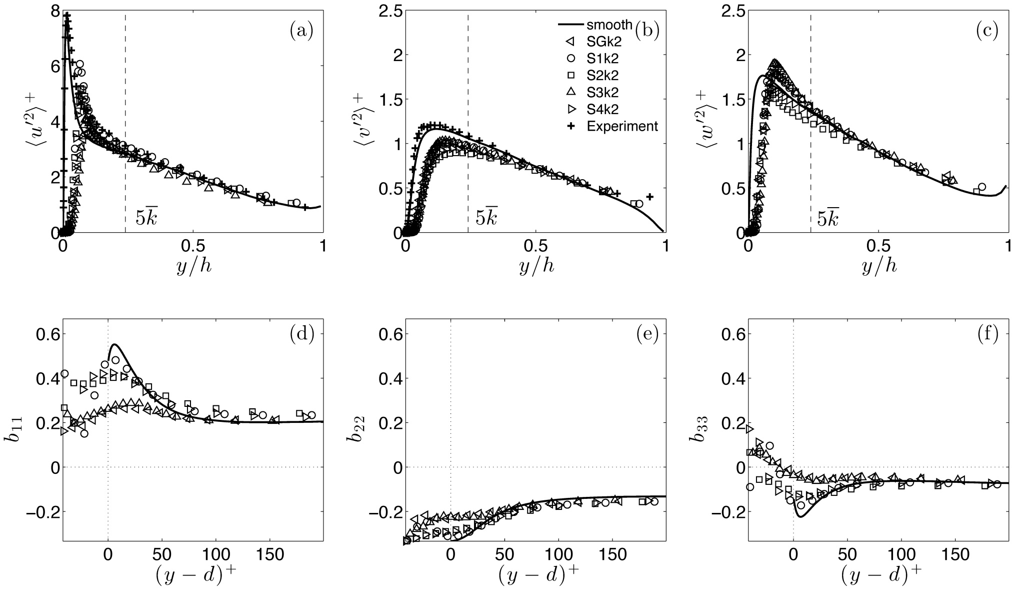

Figure 4. (a)–(c) Reynolds normal stresses for cases with k_2 and $Re_\tau = 1000$, compared with the smooth case; – – – $y = 5\overline{k}$. (d)–(f) Normal components of the anisotropy tensor of the Reynolds stresses near the wall.

3.1. *Mean flow and turbulent stresses*

The profiles of U are shown in Figure 3. The zero-plane displacement, d, is subtracted from the wall-normal location to collapse the logarithmic regions of the smooth and rough cases. The calculation of d can be found in Yuan and Piomelli [27]; for all surfaces studied, $d \approx \overline{k}$. The smooth-wall profile in the current LES collapses with the experimental data obtained by Schultz and Flack [32]. In the logarithmic region, the rough-wall profiles display an offset from the smooth-wall profile, with the amount of the displacement, ΔU^+, depending on the surface topography.

The normal components of the Reynolds stress tensor are shown in Figure 4(a–c), compared to the experimental results [32]. In the rough-wall cases, the peaks of the normal stresses move slightly away from the wall due to the displacement effect of the roughness on the mean flow; the peak magnitude of $\langle u'^2 \rangle^+$ is significant damped, a phenomenon widely observed in experiments [29] and simulations [13, 28]. Farther away from the wall, the profiles collapse, consistent with outer-layer similarity; the roughness sublayer, defined here as the layer in which roughness

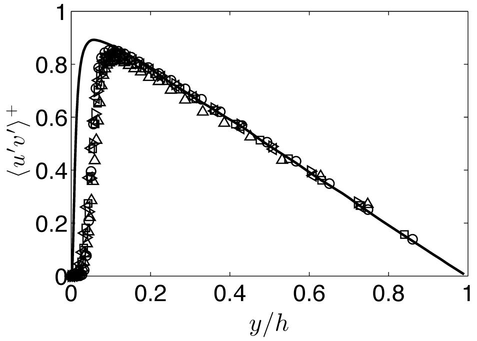

Figure 5. Reynolds shear stress for cases with k_2 and $Re_\tau = 1000$, compared with the smooth case.

alters the profiles of the normal Reynolds stresses, is confined to the region $y \lesssim 5\overline{k}$ for all surfaces.

Insights on the topographical effects can be obtained from the anisotropy of Reynolds stresses near the wall (Figure 4(d–f)). The normal components of the Reynolds stress anisotropy tensor are

$$b_{\alpha\alpha} = \frac{\langle u_\alpha u_\alpha \rangle}{\langle u_i u_i \rangle} - \frac{1}{3}, \tag{14}$$

with no summation over greek indices. In the vicinity of a smooth wall, the vertical velocity fluctuation v' is significantly damped ($(\langle v'^2 \rangle^+(0) = 0$ and thus $b_{22}(0) = -1/3$), while almost all the TKE resides in u' and w'. On a rough wall, however, v' and w' can be significant near the wall at $y \approx d$, especially for the SG and S3 surfaces, resulting in more isotropic distributions of TKE. The very different levels of near-wall augmentations of v' and w' reflect dramatic differences in the way various roughness types affect the flow.

The Reynolds shear stress profiles are compared in Figure 5. Despite the significant topographical effects in near-wall Reynolds stress anisotropy, the effect on the Reynolds shear stress is only a slight change of the shape in the roughness sublayer: different surfaces correspond to different distribution of the total drag.

3.2. *Calculation of k_s*

Since the linear relation between k_s and $\overline{k}$ is valid only inside the fully rough regime, the beginning of this regime needs to be first identified. A range of $\overline{k}^+$ is achieved with various Reynolds numbers and $\overline{k}/h$, and ΔU^+ is obtained from the mean-velocity profiles and plotted in Figure 6(a). The start of the logarithmic relation between ΔU^+ and $\overline{k}^+$ is the start of the fully rough regime, where the viscous length scale becomes unimportant, and the mean velocity $U(y)^+$ scales with y/k_s in the logarithmic region,

$$\frac{1}{\kappa} \ln y^+ + 5.0 - \Delta U^+ = \frac{1}{\kappa} \ln \left(\frac{y}{k_s} \right) + 8.5. \tag{15}$$

The logarithmic region is identified as the plateau region of $y^+(dU^+/dy^+)$. k_s is calculated from Equation (15) once ΔU^+ is obtained; its values are used to plot the roughness function in Figure 6(b); all curves asymptote to a single line in the fully rough regime. The critical roughness Reynolds number $k^+_{s,cri}$, marking the start of the fully rough regime, and the ratio $k_s/\overline{k}$ for all surfaces are tabulated in Table 3.

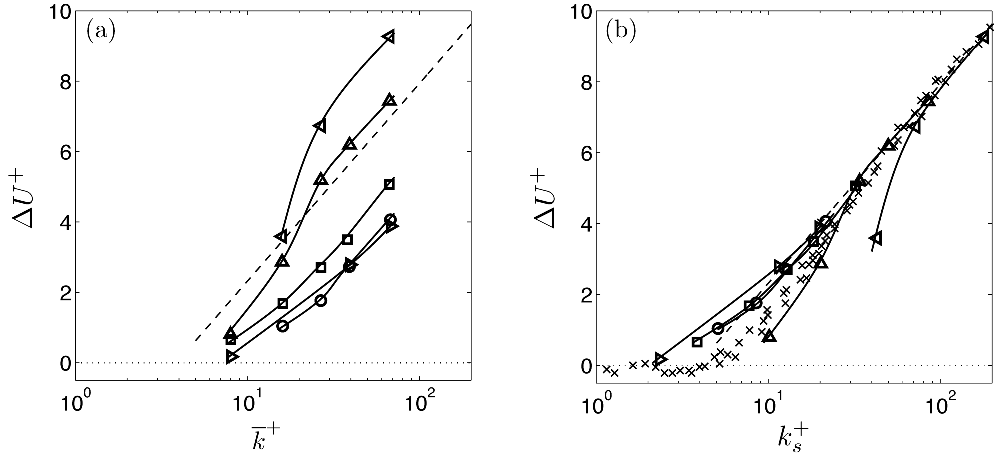

Figure 6. Dependence of roughness function on the roughness Reynolds numbers based on (a) average height and (b) equivalent sand-grain height. - - - $\Delta U^+ = 1/\kappa \ln k_s^+ - 3.5$, ◁ SG , ○ S1, □ S2, △ S3, ▷ S4, × Nikuradse sand grains [15]. Lines are for visual aid only.

Table 3. $k_s/\overline{k}$ and the start of fully rough regime ($k_{s,cri}^+$) for all surface types.

Surfaces	SG	S1	S2	S3	S4
$k_{s,cri}^+$	≈ 80	≈ 20	≈ 30	≈ 40	≈ 20
$k_s/\overline{k}$	2.68	0.32	0.48	1.27	0.29

$k_s/\overline{k}$ varies significantly (from 0.3 to 2.7), and the fully rough regime starts at a lower $k_{s,cri}^+$ for realistic surfaces (especially S1 and S4) than for SG, where it is established for $k_{s,cri}^+ \approx 80$. Earlier establishment of fully rough regime for realistic surfaces was also observed by Langelandsvik *et al.* [33], who found $k_{s,cri}^+$ to be 18 on commercial steel pipe. The roughness function for Nikuradse sand grains is also compared in Figure 6(b). It shows around the same $k_{s,cri}^+$ as Scotti's sand-grain model, SG, but its profile does not collapse with that of SG, indicating that the SG model does not reproduce precisely the uniform sand-grain surface. This is probably because the SG model was calibrated with uniform sand grains in the transitionally rough regime only [28].

The length scale k_s, however, does not collapse the roughness function for all surfaces in the transitionally rough regime; S1, S2 and S4 present a gradual increase of ΔU^+, while SG and S3 show a much more sudden growth. These results are consistent with the phenomena previously observed that modelled roughness with large distinct elements shows a delayed and more sudden increase of ΔU^+, while surfaces with a wider spectrum of scales are more likely to display a smoother increase of drag [3], since different surface scales are gradually triggered one after another to contribute to the drag as the Reynolds number increases.

3.3. *Evaluation of k_s correlations*

To evaluate the existing k_s correlations, the fully rough data are used, namely, the $k_s/\overline{k}$ values obtained from the cases with $\overline{k}/h = 0.067$ and $Re_\tau = 1000$ on all surfaces. Figure 7 shows the relation between the roughness function and ES (filled symbols). ΔU^+ does not correspond one-to-one to ES, due to the effects of other surfaces parameters, such as $k_{\rm rms}$ and s_k; for example, S2k3 and S4k3 have the same ES but differ by 30% in ΔU^+. Nevertheless, a general dependence of ΔU^+ on ES is observed for all k_3 cases, indicating that the current surfaces are in

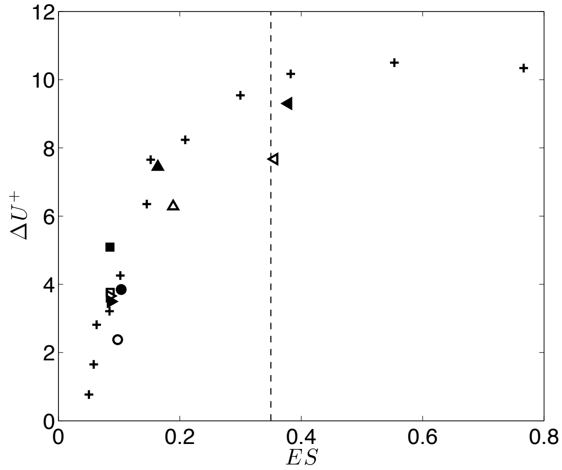

Figure 7. Dependence of the roughness function on the effective slope on various surfaces with $\overline{k}/h = 0.04$ (clear symbols) and $\overline{k}/h = 0.067$ (filled symbols); $Re_\tau = 1000$. + Napoli *et al.* [24], - - - $ES = 0.35$. Current surfaces: ◁ SG, ◯ S1, ☐ S2, △ S3, ▷ S4.

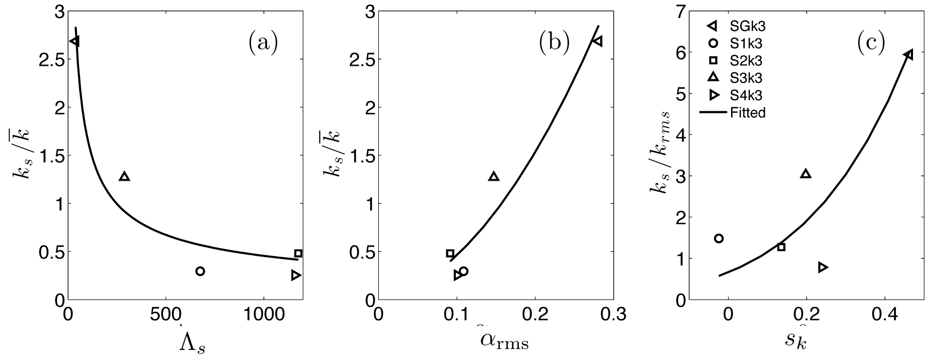

Figure 8. Actual values of k_s and fitted correlations: (a) slope/shape method, (b) slope-rms method, and (c) moments method.

the waviness regime. The cases with a lower average height, k_2, are also plotted for comparison (clear symbols), showing the dependence of ΔU^+ on $\overline{k}^+$. Also plotted are the results of numerical experiment by Napoli *et al.* [24] on a different type of roughness (composite of sinusoidal waves) with a nearly constant average height; the dashed line indicates the critical value of ES marking the end of the waviness regime; for their surfaces, this value is around 0.35. The current surfaces show the same behaviour in the waviness regime, but the range of ES is not large enough to investigate the critical ES for these surfaces.

The correlations of the forms specified in Equations (3) (slope/shape method), (5) (slope-rms method), and (6) (moment method) are considered; for each correlation, the constants a and b are fitted with the five data points, and the resultant correlation is plotted in Figure 8. Figures 8(a) and 8(b) show the slope-based correlations; the forms of these two correlations are found to represent reasonably well the variation of the current data. Larger scatter is found when the moment method is used (Figure 8(c)). In particular, surfaces S3 and S4 have similar $k_{\mathrm{rms}}/\overline{k}$ (within 22%) and s_k (within 20%) as shown in Table 1, but differ by a factor of 4 in $k_s/\overline{k}$; this is probably due to the fact that moments of height statistics do not contain slope information directly. Thus the moment-based correlation is not suitable for the surfaces whose slope is an important parameter, *i.e.*, in the waviness regime.

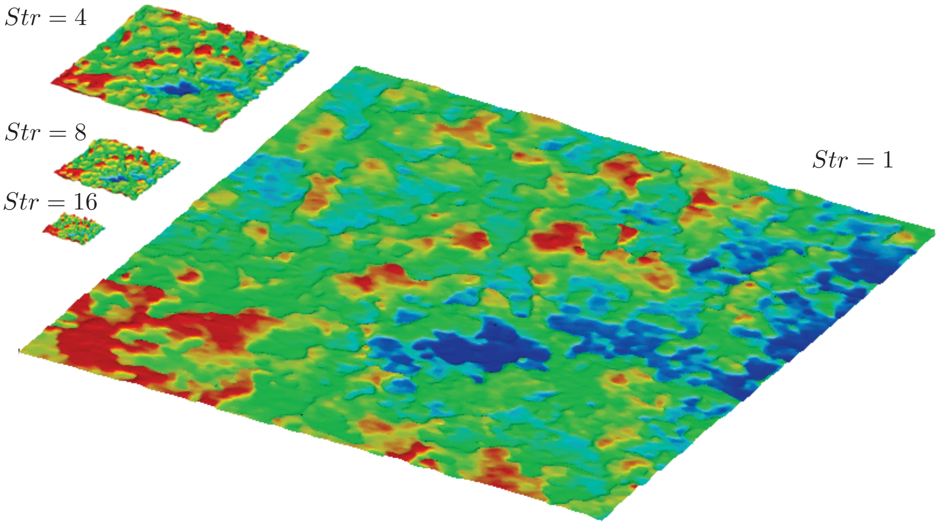

Figure 9. Artificial compressing of S2 to modify ES while keeping the same average height. One tile is shown.

Table 4. S2 surfaces with various stretching factors, Str. $Re_\tau = 1000$, $\overline{k}/h = 0.067$.

Case	Str	points per λ (in x, z)	total grids ($n_i \times n_j \times n_k$)	ES
S2Str1	1	9×9	$256 \times 213 \times 256$	0.09
S2Str4	4	7×7	$512 \times 213 \times 256$	0.18
S2Str8	8	5×5	$384 \times 213 \times 256$	0.35
S2Str16	16	5×5	$640 \times 213 \times 384$	0.70

3.4. *Critical ES*

To find out whether the range of waviness regime is the same for all surfaces, higher values of ES needs to be reached. We systematically vary ES by artificially compressing the tiles of surface S2k3 in the x- and z-directions, while keeping the size in y unchanged (Figure 9). The stretching factor, Str, is defined as the ratio of the original horizontal dimension to its final value after compression. Str is chosen to be 4, 8, and 16. Table 4 presents the spatial resolutions and resulting ES. For higher Str, more roughness patches are required to fill the flow domain; therefore, a lower surface resolution was used to limit the computational costs. However, such coarsening affects $k_{\mathrm{rms}}/\overline{k}$ and s_k by only 0.1% and 0.5%, respectively; it does, however, decrease ES by 9% for S2Str4 and by 25% for S2Str16. The grid coarsening is not expected to affect significantly the prediction of k_s, since the sensitivity of ΔU^+ to ES tends to saturate at high values of ES (as will be shown), at which point $k_{\mathrm{rms}}/\overline{k}$ and s_k play the dominant role in determining ΔU^+ [6].

The effect of ES on the roughness function obtained from the stretched surfaces is shown in Figure 10. Note that, unlike in Figure 7, the data points here correspond to surfaces that differ only in the slope (but not in k_{rms} or s_k). For surface S2, the saturation of the ES effect occurs at a much higher ES value than for the more regular roughness (pyramids) and the 2D waves previously studied [6, 24]: the plateau of $k_s/\overline{k}$ is approached for $ES \approx 0.7$, compared to the critical value of 0.35 previously found [24]. This indicates that the topographical details significantly affect separation between the waviness and roughness regimes. The wider waviness regime observed for realistic roughness is linked to its multi-scale nature: surface structures of larger wavelengths contribute to the waviness of the surface; the stronger sheltering effects of the large-scale protuberances on those of smaller ones lead to a delay in the contribution of the small-scale structures to the increase of

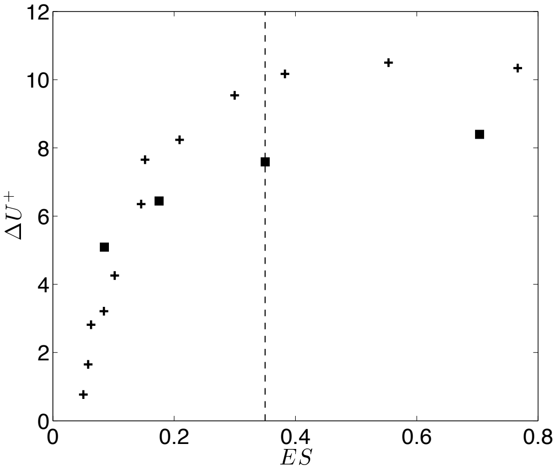

Figure 10. Variation of the roughness function as the original S2 surface is compressed by the stretching factors of 4, 8 and 16. ■ Current surfaces, + Napoli *et al.* [24], - - - $ES = 0.35$.

friction.

4. Conclusions

Four types of realistic roughness with different topographical characteristics and the sand-grain roughness are compared. Their effects on the mean flow and turbulent stresses are studied using large-eddy simulations in an open-channel flow configuration. The beginning of the fully rough regime is identified for each surface, and within this regime, k_s is determined by matching the measured roughness function to that of the uniform sand grain of Nikuradse. The ratio between k_s and the average roughness height, $\overline{k}$, is shown to depend on the roughness type.

The current surfaces are shown to be in the waviness regime defined by Schultz and Flack [23]. The resulting $k_s/\overline{k}$ is then used to evaluate the performance, in this regime, of three existing forms of k_s-correlations that predict k_s based solely on the surface information; these include correlations based on slope/shape parameter, on slope-rms, and on moments of height statistics. The slope-based correlations yield collapse of data, while the moment-based correlation gives wider scatter, since the moments do not contain slope information and thus do not scale $k_s/\overline{k}$ in the cases where the surface slope is an important parameter.

The effective slope (ES) categorizes rough surfaces according to the importance of the surface slope to the roughness function; thus it offers a guideline in choosing k_s-correlations for an arbitrary rough topography. Of crucial importance is the critical ES that separates the waviness and roughness regimes. By artificially compressing a realistic surface and systematically increasing ES, we found that the critical ES of a realistic surface can be much higher than the value of 0.35 found for pyramid roughness and 2D wave-composite. Future studies are required to study and model the dependence of the critical ES on roughness topography.

Acknowledgements

Support from Hydro Québec, the Natural Science and Engineering Research Council of Canada (NSERC), and the High Performance Computing Virtual Laboratory (HPCVL) is acknowledged. Professor Alberto Scotti is thanked for the code gen-

erating the volume fraction for the immersed boundary method.

References

[1] J.P. Bons, R.P. Taylor, S.T. McClain, and R.B. Rivir, *The many faces of turbine surface roughness*, J. Turbomach. 123 (2001), pp. 739–748.
[2] M.R. Raupach, R.A. Antonia, and S. Rajagopalan, *Rough-wall boundary layers*, Appl. Mech. Rev. 44 (1991), pp. 1–25.
[3] J. Jiménez, *Turbulent flows over rough walls*, Annu. Rev. Fluid Mech. 36 (2004), pp. 173–196.
[4] J.P. Bons, *St and C_f augmentation for real turbine roughness with elevated freestream turbulence*, J. Turbomach. 124 (2002), pp. 632–644.
[5] Y. Wu, and K.T. Christensen, *Reynolds-stress enhancement associated with a short fetch of roughness in wall turbulence*, AIAA J. 44 (2006), pp. 3098–3106.
[6] K.A. Flack, and M.P. Schultz, *Review of hydraulic roughness scales in the fully rough regime*, J. Fluids Eng. 132 (2010), pp. 041203–1—10.
[7] Y. Wu, and K.T. Christensen, *Outer-layer similarity in the presence of a practical rough-wall topography*, Phys. Fluids 19 (2007), pp. 085108–1—15.
[8] Y. Wu, and K.T. Christensen, *Spatial structure of a turbulent boundary layer with irregular surface roughness*, J. Fluid Mech. 655 (2010), pp. 380–418.
[9] B.E. Johnson, and K.T. Christensen, *Turbulent flow over low-order models of highly irregular surface roughness*, AIAA J. 47 (2009), pp. 1288–1299.
[10] R. Mejia-Alvarez, and K.T. Christensen, *Low-order representations of irregular surface roughness and their impact on a turbulent boundary layer*, Phys. Fluids 22 (2010), pp. 015106–1—20.
[11] A.M. Licari, and K.T. Christensen, *Modeling cumulative surface damage and assessing its impact on wall turbulence*, AIAA J. 49 (2011), pp. 2305–2320.
[12] W. Anderson, and C. Meneveau, *Dynamic roughness model for large-eddy simulation of turbulent flow over multiscale, fractal-like rough surfaces*, J. Fluid Mech. 679 (2011), pp. 288–314.
[13] A. Busse, C.J. Tyson, and N.D. Sandham, *Direct numerical simulation of turbulent channel flow over engineering rough surfaces*, in *Turbulent shear flow phenomena 8*, 2013.
[14] J.P. Bons, S.T. McClain, Z.J. Wang, X. Chi, and T.I. Shih, *A comparison of approximate versus exact geometrical representations of roughness for CFD calculations of C_f and St*, J. Turbomach. 130 (2008), pp. 021024–1—10.
[15] J. Nikuradse, *Laws of flow in rough pipes*, NACA Technical Memorandum 1292 (1933).
[16] J.P. Bons, *A review of surface roughness effects in gas turbines*, J. Turbomach. 132 (2010), pp. 021004–1—16.
[17] A. Sigal, and J.E. Damberg, *New correlation of roughness density effects on the turbulent boundary layer*, AIAA J. 28 (1990), pp. 554–556.
[18] J.A. van Rij, B.J. Belnap, and P.M. Ligrani, *Analysis and experiments on three-dimensional, irregular surface roughness*, J. Fluids Eng. 124 (2002), pp. 671–677.
[19] F.A. Dvorak, *Calculation of turbulent boundary layers on rough surfaces in pressure gradient*, AIAA J. 7 (1969), pp. 1752–1759.
[20] R.L. Simpson, *A generalized correlation of roughness density effects on the turbulent boundary layer*, AIAA J. 11 (1973), pp. 242–244.
[21] R. Dirling, *New correlation of roughness density effects on the turbulent boundary layer*, AIAA J. (1973), pp. 73–763.
[22] J.P. Bons, *A critical assessment of Reynolds analogy for turbine flows*, J. Heat Transfer 127 (2005), pp. 472–485.
[23] M.P. Schultz, and K.A. Flack, *Turbulent boundary layers on a systematically varied rough wall*, Phys. Fluids 21 (2009), pp. 015104–1—9.
[24] E. Napoli, V. Armenio, and M. De Marchis, *The effect of the slope of irregularly distributed roughness elements on turbulent wall-bounded flows*, J. Fluid Mech. 613 (2008), pp. 385–394.
[25] C. Meneveau, T.S. Lund, and W.H. Cabot, *A Lagrangian dynamic subgrid-scale model of turbulence*, J. Fluid Mech. 319 (1996), pp. 353–385.
[26] A. Keating, U. Piomelli, K. Bremhorst, and S. Nešić, *Large-eddy simulation of heat transfer downstream of a backward-facing step*, J. Turbul. 5 (2004), pp. 20–1—27.
[27] J. Yuan, and U. Piomelli, *Numerical simulations of sink-flow boundary layers over rough surfaces*, Phys. Fluids 26 (2014), pp. 015113–1—015113–28.
[28] A. Scotti, *Direct numerical simulation of turbulent channel flows with boundary roughened with virtual sandpaper*, Phys. Fluids 18 (2006), pp. 031701–1—4.
[29] R.J. Volino, M.P. Schultz, and K.A. Flack, *Turbulence structure in a boundary layer with two-dimensional roughness*, J. Fluid Mech. 635 (2009), pp. 75–101.
[30] D.G. Bogard, and D.L. Schmidt, *Characterization and laboratory simulation of turbine airfoil surface roughness and associated heat transfer*, J. Turbomach. 120 (1998), pp. 337–342.
[31] R.B. Dean, *Reynolds number dependence of skin friction and other bulk flow variables in two-dimensional rectangular duct flow*, ASME J. Fluids Eng. 100 (1978), pp. 215–223.
[32] M.P. Schultz, and K.A. Flack, *Reynolds-number scaling of turbulent channel flow*, Phys. Fluids 25 (2013), pp. 025104–1—13.
[33] L.I. Langelandsvik, G.J. Kunkel, and A.J. Smits, *Flow in a commercial steel pipe*, J. Fluid Mech. 595 (2008), pp. 323–339.